Research Article Vol. 5, No. 4 / April 2018 / Optica 320

optica

Regional trace-gas source attribution using a field-deployed dual frequency comb spectrometer

Sean Coburn,[1,*,†] Caroline B. Alden,[1,2,6,†] Robert Wright,[1] Kevin Cossel,[3] Esther Baumann,[3] Gar-Wing Truong,[3] Fabrizio Giorgetta,[3] Colm Sweeney,[2,4] Nathan R. Newbury,[3] Kuldeep Prasad,[5] Ian Coddington,[3] and Gregory B. Rieker[1,7]

[1]Precision Laser Diagnostics Laboratory, University of Colorado Boulder, Boulder, Colorado 80309, USA
[2]Cooperative Institute of Research in Environmental Sciences, Boulder, Colorado 80309, USA
[3]National Institute of Standards and Technology, Boulder, Colorado 80305, USA
[4]National Oceanic and Atmospheric Administration, Boulder, Colorado 80305, USA
[5]National Institute of Standards and Technology, Gaithersburg, Maryland 20899, USA
[6]e-mail: aldenc@colorado.edu
[7]e-mail: greg.rieker@colorado.edu
*Corresponding author: coburns@colorado.edu

Received 9 January 2018; revised 21 February 2018; accepted 22 February 2018 (Doc. ID 319377); published 22 March 2018

Identification and quantification of trace-gas sources is a major challenge for understanding and regulating air quality and greenhouse gas emissions. Current approaches provide either continuous but localized monitoring, or quasi-instantaneous "snapshot-in-time" regional monitoring. There is a need for emissions detection that provides both continuous and regional coverage, because sources and sinks can be episodic and spatially variable. We field deploy a dual frequency comb laser spectrometer for the first time, enabling an observing system that provides continuous detection of trace-gas sources over multiple-square-kilometer regions. Field tests simulating methane emissions from oil and gas production demonstrate detection and quantification of a 1.6 g min^{-1} source (less than the average emissions from a small pneumatic controller) from a distance of 1 km, and the ability to discern two leaks among a field of many potential sources. The technology achieves the goal of detecting, quantifying, and attributing emissions sources continuously through time, over large areas, and at emissions rates ~1000 × lower than current regional approaches. It therefore provides a useful tool for monitoring and mitigating undesirable sources and closes a major information gap in the atmospheric sciences.

OCIS codes: (010.0280) Remote sensing and sensors; (300.1030) Absorption; (280.1120) Air pollution monitoring.

https://doi.org/10.1364/OPTICA.5.000320

1. INTRODUCTION

Emissions of greenhouse gases and pollutants pose serious risks for global climate change and human health and safety. Regional detection, quantification, and attribution of trace gas sources and sinks is therefore a critical need for a variety of applications, including quantification of emissions in urban or industrial settings for monitoring, reporting, and verification; detection of small amounts of hazardous gases; verification of sub-surface sequestration efforts; and characterization of the exchange of trace gases between the atmosphere and natural or managed ecosystems. For many needs, strictly local and/or strictly time-invariant observational capabilities do not suffice for complete characterization of fluxes. For example, the "snapshots-in-time" provided by aircraft, satellite, or vehicle-mounted point sensor estimations of emissions from oil and gas operations may miss the largest fluxes, which are thought to be highly infrequent [1,2] or may misrepresent fluxes by sampling during midday, when manually triggered (operational) emissions are most frequent [3]. Similarly, regional continuous monitoring can be achieved with networks of point sensors, but the level of detail in the disaggregation of source locations and sizes must necessarily scale with the number of sensors deployed (e.g., [4]), increasing costs and complexity.

Here, we demonstrate a technology capable of continuous monitoring of trace gas fluxes, with the ability to distinguish between emissions sources at fine scales and across large areas and to infer time evolution and variability of individual sources. We present the first remote field deployment of dual frequency comb technology [5,6], coupled with innovations in atmospheric inversion modeling, to enable the continuous detection, location and quantification of small trace gas sources over several square kilometer regions using a single, autonomous instrument. The system consists of the fielded dual frequency comb spectrometer, located in a centralized mobile trailer, which emits a sparse array of kilometer-scale beams strategically located throughout a region

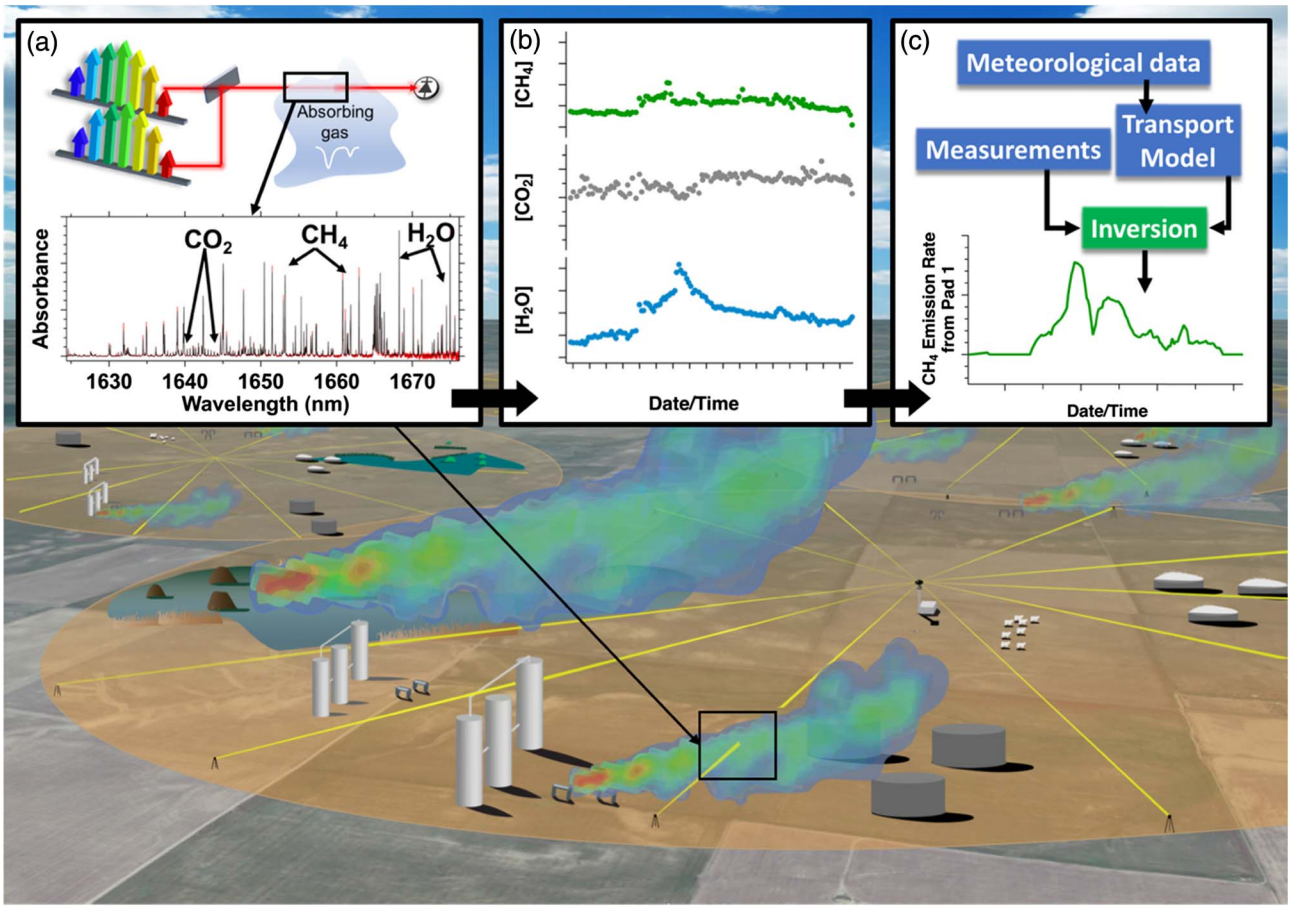

Fig. 1. Regional source monitoring with a centralized DCS. (a) The DCS measures trace gas absorption over an array of long-distance beam paths. (b) Time-resolved trace gas concentrations are determined from fits to the absorption spectra with ppb-km sensitivity and stability. (c) An atmospheric transport model and inversion determines source location and time-resolved emission rate.

of potential emitters to sensitively measure trace gas concentrations over time (see Fig. 1). The measurements are coupled with an atmospheric transport model in a Bayesian inversion to identify sources and quantify the emission rate over time at each source location with several-minute resolution. The laser beam is invisible and eye-safe, and the system can operate continuously day and night except during periods of total optical occlusion (e.g., heavy precipitation). Trace gas sources do not need to be imaged directly, which is important for cases in which line-of-sight from the laser to the source location is blocked by terrain or vegetation. Rather, the sensitivity of the spectrometer enables a sparse beam array that only must intersect the plumes downwind of the sources.

Two field test scenarios utilizing controlled methane emissions are presented here to demonstrate the system's capabilities with respect to two key features for regional trace gas emission characterization: 1) quantification of small, variable-rate gas sources from long distance (>1 km); and 2) identification and quantification of multiple sources within a field of many potential sources. During the first test scenario, we quantify an emission source varying from 1.6 to 8 $g\,min^{-1}$ over a 24 h period from a distance of >1 km. As a point of reference, the average breathing rate for an adult human can be estimated at ~8 standard liters per minute (slpm, air), compared with volumetric rates ranging from 2.5 to 12 slpm (methane) used for the emission tests in this study. The average reported emissions from pneumatic controllers found on well pads also falls within this range [1,7]. During the second test, we show that the system correctly identifies and quantifies two simultaneous emission sources among an area with up to five potential sources.

2. FIELD-DEPLOYED DUAL-COMB SPECTROMETER

The frequency comb laser is based on Nobel-prize-winning research [8,9] that has significantly impacted the field of molecular spectroscopy [10–12]. The femtosecond pulsed output of a mode-locked frequency comb laser is composed of thousands of perfectly spaced, discrete wavelength elements or "comb teeth," that act as a parallel set of continuous-wave lasers with known frequencies. Dual frequency comb spectroscopy uses two combs with slightly different tooth spacing, mixed on a photodiode after transmission through a sample, to extract high resolution absorption information [13–17,11]. The result is an unprecedented combination of spectral bandwidth (>100 nm, 12 THz) and resolution ($<2 \times 10^{-3}$ nm, 200 MHz), providing precise and accurate absorption spectra over long atmospheric paths [18,19].

Achieving field operation of the dual-comb spectrometer (DCS) under harsh conditions required several technological advancements over the laboratory-based proof-of-concept open-path DCS [18]. The original ring-cavity frequency combs relied

on nonlinear polarization rotation mode locking and were extremely sensitive to vibration and any environmental change that manipulated the polarization state within the cavity. The dual-comb spectrometer employed here utilizes a linear-cavity frequency comb design with all polarization-maintaining fiber and mode locking based on a semiconductor saturable absorber mirror (SESAM) [5,20]. The new frequency comb design was shown to be far more robust and capable of operation in a moving vehicle [5]. Phase coherence between the two frequency combs, and full stabilization of the frequency comb teeth in the original laboratory-based system, was achieved by phase locking the combs to two fiber lasers that were locked to a temperature-stabilized cavity under vacuum. This system was both expensive and sensitive to vibration and environmental changes. Stabilization of the fieldable system demonstrated here is achieved by locking the carrier offset frequency (f_{ceo}) using f-to-$2f$ locking, and phase locking an individual tooth from each comb to a common 1 kHz linewidth continuous-wave (CW) commercial diode laser. The diode laser is then stabilized against drift through a feedback loop to the drive current or diode temperature using the repetition rate of one of the combs [6]. A commercially available ovenized quartz oscillator with high stability and low drift serves as the time base for all electronic components. These measures allow the DCS system to operate untethered from laboratory frequency references required by the proof-of-concept instrument, while still maintaining a level of stabilization that allows for the high-fidelity measurements presented here.

The near-infrared (NIR) frequency comb oscillators used here generate light around 1.55 μm over a ~10 nm range. The light from each oscillator is amplified and spectrally broadened (using highly nonlinear fiber) to cover from 1.0 to 2.2 μm (for f-to-$2f$ locking). The light from the two combs is then combined and spectrally filtered using a custom fiberized interference filter so that only light in the 1.62–1.69 μm region is sent over the open path (an optimal NIR wavelength range for measurement of atmospheric CH_4 and water vapor over long paths with high precision). The filtered light is then transmitted via 20 m of single-mode fiber (SMF) to the telescope transceiver, which is located either on top of the spectrometer trailer or on a standalone tower nearby. The transceiver sends light to and receives light from the retroreflectors, which are placed in the field, as demonstrated here, or can be located on an unmanned aerial system as in [21].

A single 100-MHz-bandwidth InGaAs photodetector mounted on the telescope transceiver is used for detection of the dual-comb interference signal. The detector signal is transmitted to the data collection system inside the mobile laboratory. A bias tee separates the RF and DC components of the signal. The DC portion is used to monitor the power reaching the detector. The RF portion is passed to the data collection system and digitized at 14 bits and 200 MHz (clocked at the repetition rate of one of the combs). Prior to digitizing, the dual-comb signal is amplified and attenuated in order to optimize linearity of the detection system [19]. The digitizer is controlled by a custom acquisition code that allows for real-time averaging of individual interferograms as well as phase correction and additional averaging of phase-corrected interferograms in order to reduce the final data burden. For these tests, individual interferograms are recorded at ~630 Hz and averaged for 128 s with phase corrections applied to the interferograms every 150 ms. An example transmission spectrum from the DCS is shown in Fig. 2(a).

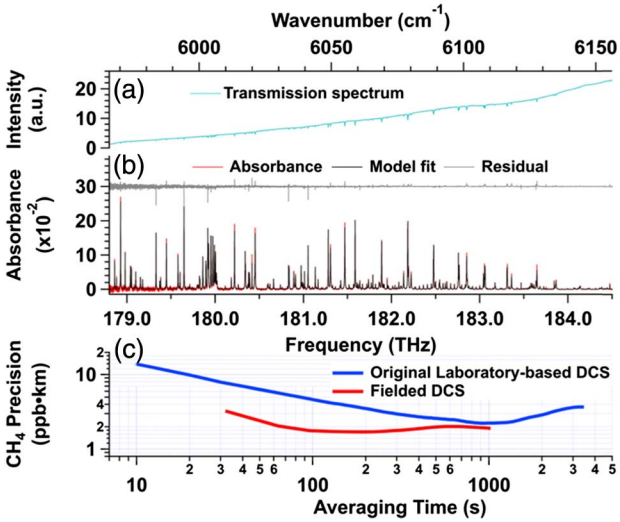

Fig. 2. (a) Raw transmission spectrum. (b) Result of fit with absorbance model including CH_4, CO_2, and H_2O. The fit residual is largest near water vapor features in the spectrum. (a) and (b) share horizontal axes. (c) Allan deviation for methane mole fraction data collected during well-mixed atmospheric conditions and without nearby leak sources. Also included in (c) is an Allan deviation trace from open-path DCS measurements using the original laboratory-based system [13].

The spectra are fit with an absorption model (based on the HITRAN database in this case) to simultaneously retrieve the atmospheric concentration of all trace gases that absorb within the bandwidth [Fig. 2(b)]. The combination of the dual-comb instrument and fitting approach produces results that are undistorted by atmospheric turbulence, free from instrument-specific lineshapes, robust against species interference, and require no periodic calibration (the absorption model serves as the permanent calibration for all instruments) [18,19]. Cross validations between this DCS instrument and another using the same fieldable design show a long-term agreement of 0.35% (7 ppb) in CH_4 concentration [19]. Thus, the instruments can be networked and the measurements linked (through an appropriate absorption model) to international standards without periodic calibration.

Figure 2(c) shows the instrument precision versus averaging time (Allan deviation) for methane measurements with the fielded DCS under windy well-mixed conditions. This gives an indication of the DCS performance and optimal averaging time under ideal conditions. The measurements used for the Allan deviation calculation were taken without a leak present, during a 6 h period when the atmospheric variability in background methane was very low, which is necessary to accurately decouple instrument performance from natural atmospheric variations. The methane measurement precision is compared with results from the original laboratory-based system under similar conditions. The fielded DCS system is shown to be more precise, reaching below 2 ppb · km sensitivity in 100 s. The improvement in precision is mostly the result of improved transceiver throughput over the laboratory-based setup (see Supplement 1 for further details). This performance compares well with other work using a similar DCS architecture [6,19,22].

The current spectrometer is capable of detecting a range of near-infrared absorbing molecules such as CH_4, H_2O, CO_2,

and isotopologues. With modifications, it would be capable of detecting O_2, SO_2, NH_3, and CO. More complex comb spectrometers operating further into the mid-infrared will expand the list of detectable molecules in the future [23].

3. TIME-RESOLVED INVERSION OF THE DCS DATA TO LOCATE AND SIZE TRACE-GAS SOURCES

New inversion techniques are needed to provide time-resolved location and quantification of sources with the sparse array of line-of-sight integrated open-path measurements provided by the DCS. For this, we implement an inversion that identifies sources and quantifies emissions at multiple possible source locations, given a time series of observations and related covariance, a transport model to relate the sources and open-path measurements, and estimates of temporal and spatial emission and background covariance [24].

Specifically, we use a Bayesian inversion to solve for time-resolved fluxes. The technique allows for the identification of the onset and end of potentially intermittent emissions, and has not previously been employed for this type of application. We achieve time resolution that varies from several minutes to tens of minutes, depending upon the number of retroreflectors queried and measurement frequency. Following [24], the standard formulation for the mass emission rate estimate, or flux estimate, $\hat{\mathbf{s}}$, is

$$\hat{\mathbf{s}} = \mathbf{s}_p + \mathbf{QH}^T(\mathbf{HQH}^T + \mathbf{R})^{-1}(\mathbf{z} - \mathbf{Hs}_p). \quad (1)$$

The $m \times 1$ posterior flux vector is $\hat{\mathbf{s}}$. $\mathbf{s}_p$ is the $m \times 1$ state vector of prior source estimates, $\mathbf{z}$ is the $n \times 1$ vector of observations, $\mathbf{R}$ is the $n \times n$ matrix of observation covariance, $\mathbf{Q}$ is the $m \times m$ matrix of prior flux covariance, and $\mathbf{H}$ is the $n \times m$ matrix of source–receptor functions. The dimension n is equal to the number of observations. The dimension m is equal to the number of mass emission rates to be estimated, which is equal to the number of time steps evaluated multiplied by the number of potential source locations to be monitored.

The inversion uses spectrometer measurements as the prior estimate for background concentrations, thereby removing potentially confounding signals from nearby emissions and obviating the need for additional sensors to constrain background conditions. A unique aspect of our approach is that background concentrations are optimized in the inversion to limit aliasing of background uncertainty onto flux estimation. Any atmospheric transport model can be used to determine the source–receptor functions. Here, we use the Gaussian plume model as a steady-state solution to atmospheric transport, such that the number of time steps of flux estimation is equal to the number of atmospheric observations, n. Assumptions of steady-state atmospheric transport, based on mean meteorological conditions during a 2 min measurement window, are an appropriate choice because the travel time (approximated using mean wind speed) from a given source location to its assigned downwind beam is comparable to measurement averaging times. Further, our use of a simplified model of atmospheric transport serves as a baseline assessment of the viability of the methodology; more advanced models can be employed in the future, which could reasonably be expected to reduce the error in the posterior leak estimate. A more detailed description of the components of the inversion can be found in Supplement 1. Additionally, there is potential to explore other numerical methods for decreasing uncertainty in derived emission rates using open-path DCS data [25].

4. RESULTS

In the initial deployment described here, we choose the important case of methane emission detection and quantification from oil and gas operations to demonstrate the capability of the system. To this end, controlled methane sources are dispersed across a field site to simulate emissions from natural gas production sites. The fielded DCS is located at the Table Mountain Field Site, ~10 km north of Boulder, Colorado (Fig. 3). A trailer houses the DCS, but the volume of the DCS and supporting equipment is 0.6 × 0.9 × 0.7 m and thus amenable to smaller platforms. The launch/receive optics and pointing gimbal are mounted on the trailer roof or an adjacent tower. Both the frequency combs and transceiver optics have been subjected to four seasons of weather over a 12 month operational period including drastic temperature variations (~18°C daily), significant wind loading (>30 ms^{-1}), and precipitation (rain, snow). Retroreflectors are placed at distances of up to 1.1 km from the spectrometer. Targeted sequentially, each retroreflector reflects laser light back to the photodetector co-located with the launch optics. The retroreflectors are placed among the potential sources (lateral offset between source and beam path is 15–60 m) for measurement of upwind and downwind integrated trace-gas concentrations along sets of laser beams, enabling the estimation of background concentrations for each potential emission site and for each time step. This configuration holds potential for identification of even very small sources in regions with a high density of oil and gas operations, where ambient concentrations of methane can have high spatial and rapid temporal variability.

First, we demonstrate the identification and quantification of a very small, variable-rate emission at a distance of 1 km (Fig. 4). Atmospheric measurements begin at 09:00 local time, and continue until 07:00 the following day. At 14:05, the controlled release of 7.7 g min^{-1} begins. At 18:00 the rate changes to 4.6 g min^{-1}, at 22:00 the rate drops again to 3.1 g min^{-1}, and at 00:00 drops to 1.6 g min^{-1}, before stopping completely at 04:55 (Fig. 4). Atmospheric CH_4 measurements downwind of the leak show clear enhancements when the controlled release begins, and the inversion successfully predicts that no leak is present before this time (the posterior flux is within $1 - \sigma$ of zero). The posterior emission estimate becomes significantly greater than zero within minutes of the true leak start, demonstrating that the system can rapidly identify the onset of emissions, a particularly important feature for intermittent sources. The posterior emission estimate remains significant for the entire leak duration, becoming indistinguishable from zero only when the controlled release is shut off at 04:55 the next day. The posterior emission rate is variable, particularly during periods of low wind speed and shifting wind directions, such as occurred between 16:00 and 20:00 (see Figs. 4 and S1), and at night, when parameterization of atmospheric stability is difficult. Use of more sophisticated transport models and parameterizations may be expected to increase the fidelity of the representation of atmospheric flow, and may therefore lead to reductions in flux estimation errors. Over the measurement period, the root-mean squared (RMS) deviation between the measured and true leak rate is 2.9 g min^{-1}. For comparison, this value is smaller than the mean emissions from functioning pneumatic controllers on a well site [1,7].

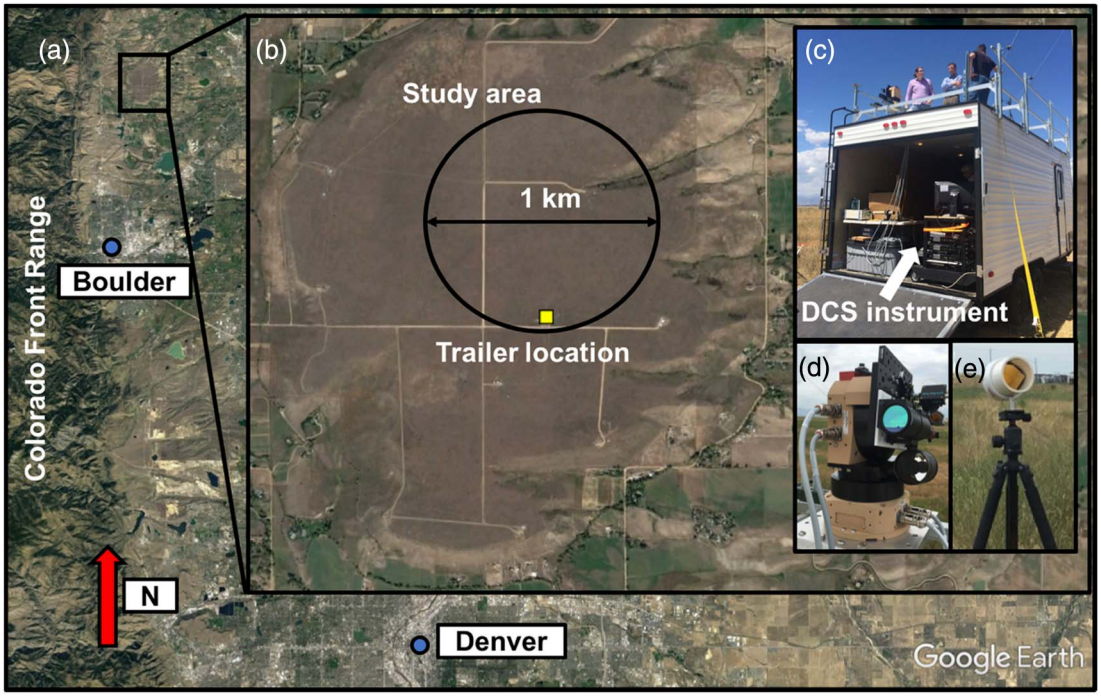

Fig. 3. Overview of the field site. (a) Table Mountain field site location. (b) Zoomed view of the site including mobile laboratory (yellow square) and the area over which tests were conducted (black circle). (c) Field deployed DCS, (d) gimbal/telescope, and (e) retroreflector.

During the period identified by the inversion as having nonzero emissions, the overall average posterior emission rate is 5.2 ± 1.6 g min^{-1}, which is within $1-\sigma$ of the true average emission rate of 4.9 g min^{-1} (Fig. 4). The rapid variability in the background methane concentration is immediately apparent in the data. Rapid increases and decreases in the overall methane concentration, e.g., at 12:00, 17:00, and 03:00, correspond with abrupt changes in the wind direction, which carries air masses from different urban, mountain, and nearby oil and gas production environments across the test site (see Fig. S1).

A second set of field tests assesses the ability of the observing system to locate and quantify simultaneous emissions from multiple sources. To simulate an accurate representation of the density of oil and gas production in the United States, the inversion is given prior knowledge of the spatial distribution of five well sites similar to a randomly selected section of the nearby Denver–Julesburg oil and gas basin. Controlled methane release points are positioned at two of five well sites (Fig. 5). Eight retroreflectors create an array of beams interspersed among the sites. Measurements begin at 09:00, and controlled releases begin at both emission points at 11:30 with equal rates of 3.1 g min^{-1}, increasing to 3.7 g min^{-1} at 13:10. Atmospheric measurements continue until both controlled releases are turned off at 17:00. The inversion identifies emissions at both sites beginning at the correct time (Fig. 5). The RMS deviation between the estimated and true leak strength is below 1.2 g min^{-1}. Equally important, the inversion also correctly identifies the three nonleaking well sites as having emissions consistent with zero. The sharp decrease in the overall methane occurring at 13:30 coincides with a shift in the wind direction, which brings in an air mass with lower background methane concentration (see Fig. S2).

These tests demonstrate that the system proved fully capable of detecting and quantifying 1) a small, variable methane emissions (1.6–8 g min^{-1}) from a distance of >1 km, and 2) two simultaneous methane emissions among a field of five potential sources. Both of these capabilities are advantageous for systems that seek to provide robust and sensitive monitoring for methane emissions in the oil and natural gas production sector.

5. DISCUSSION

The production, transport, and storage of natural gas from the more than 1 million active wells in the U.S. results in both intentional and unintentional emissions of 6–12 million metric tons of CH_4 to the atmosphere annually [26,27]. These emissions represent lost revenue, pose risks to public safety, accelerate climate change, and, through natural gas co-emissions, lead to decreased air quality [28]. The economics of leak mitigation is complicated by the wide spatial distribution and time variability of potential leaks, making the task of locating leaks with traditional optical gas imaging and handheld sensing technologies labor intensive, costly, and unreliable [29]. Existing methane sensing technologies offer high spatial but low temporal coverage or vice versa [30]. Satellite and aircraft mass balance approaches cover large regions but at coarse spatial and temporal resolution. Additionally, these methods are effective only under a subset of atmospheric conditions (e.g., clear sky) and are limited to identification of leaks greater than 1000–10,000 g min^{-1} [31–34]. Sensors mounted on vehicles require operators and offer snapshots in time [35–38]. Fixed, continuous ground-based sensors do not acquire sufficient information to locate specific sources from more than a few hundreds of meters [29], and are currently too expensive for adequate monitoring of oil and gas operations.

The dual-comb spectrometer and atmospheric inversion approach demonstrated here offers the ability to continuously and autonomously monitor many potential sources across multiple square kilometer regions with emission rates down to

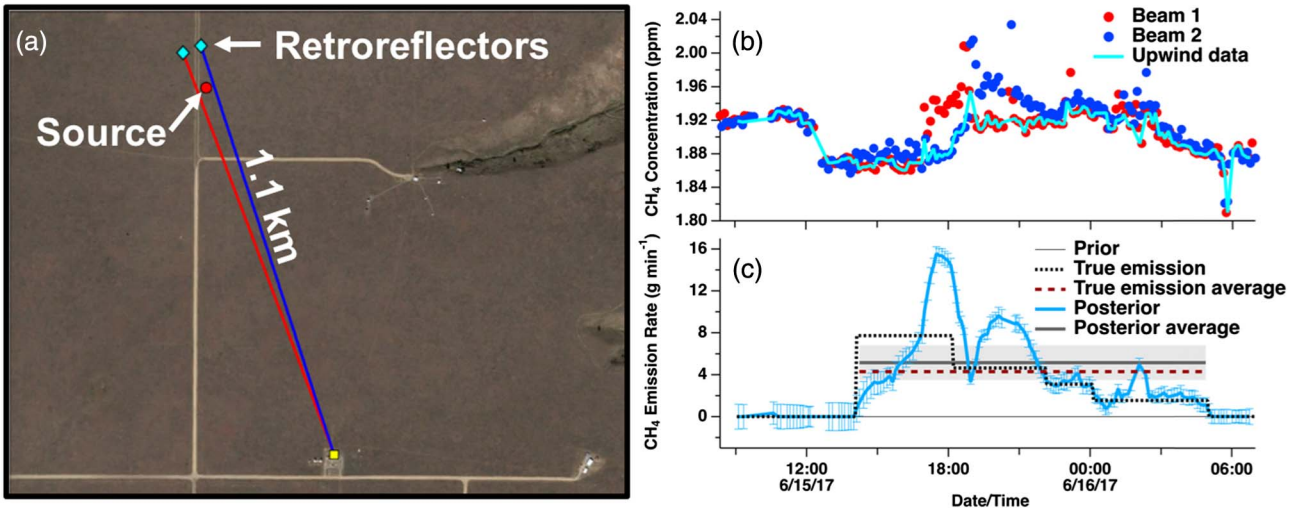

Fig. 4. Detection of a small, time-varying methane source from 1 km. (a) Map showing the site configuration including retroreflectors (blue diamonds) and source (red circle). (b) Methane concentrations measured on beam paths shown in (a). The light blue line denotes the background measurement (the upwind beam depends on wind direction). (c) Retrieved emission rate (blue line; error bars are 1 – σ posterior uncertainty), compared with true emission rate (black dotted line). Also shown is the prior estimate of the emission (thin gray line at zero) used in the inversion and the average values for both the true emission rate (maroon dashed line) and the posterior (thick gray line with mean uncertainty).

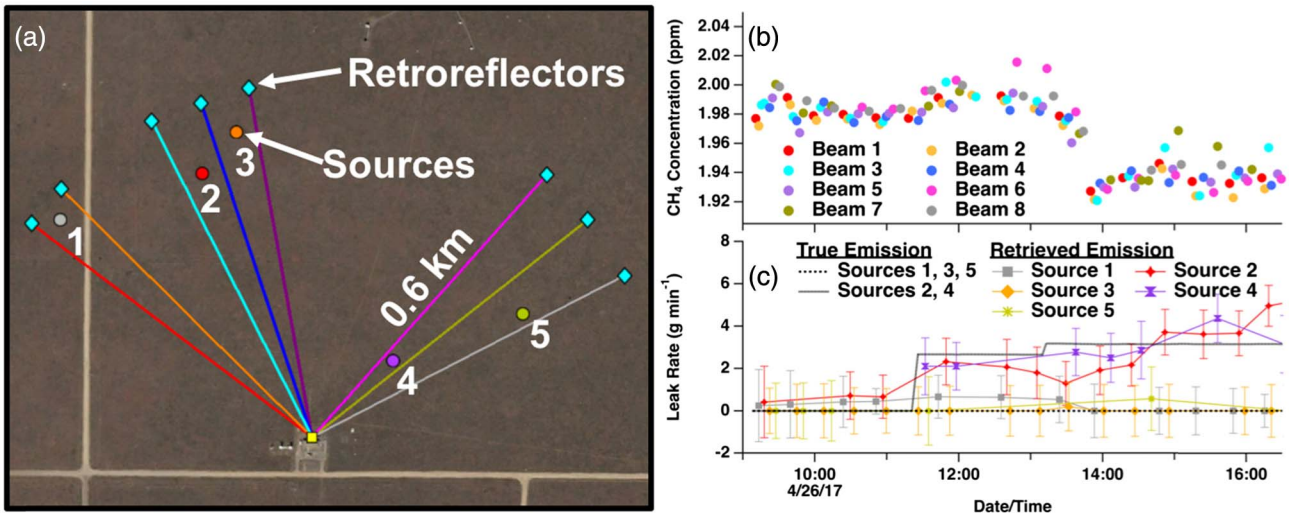

Fig. 5. Detection of two sources from among multiple potential sources. Layout of (a) and (b) in this figure follow that of Fig. 4. (c) True emission rates (sources 2 and 4, solid gray lines; sources 1, 3, and 5, dotted black lines) and retrieved emission rates (sources 1, gray squares; 2, red diamonds; 3, orange diamonds; 4, purple hourglasses; 5, gold asterisks).

1.6 g min^{-1}. Achieving this level of sensitivity means that the system is capable of detecting all sources relevant to oil and gas infrastructure, from so-called "super-emitters," or large point sources that account for a substantial portion of annual renegade emissions, to small sources <1 ton yr^{-1} (e.g., faulty pneumatic controllers). Additionally, the ability to support continuous monitoring increases the chances of detecting large (and small) episodic emission sources, for which there is currently little to no data describing the frequency of occurrence. Thus, in regions of dense oil and gas operations, this approach could lead to drastically reduced monitoring costs, enabling economically viable leak mitigation.

Future applications of the observation and inversion framework described here range from detection and quantification of trace gas sources over large urban and rural regions to sensitive early-warning systems for the presence of small amounts of airborne chemical constituents, to confirmation and monitoring of underground storage or sequestration of gaseous materials. The system bridges a critical gap in existing trace-gas monitoring capabilities by providing highly sensitive, time-varying, continuous, regional-scale coverage.

Funding. Advanced Research Projects Agency—Energy (ARPA-E) (DE-AR0000539); Office of Fossil Energy (DE-FE0029168); Defense Advanced Research Projects Agency (DARPA); National Institute of Standards and Technology (NIST).

Acknowledgment. The authors would like to thank research leaders at the Table Mountain Test Site for help with logistics and for facilitating the field deployment and research activities covered in this paper.

See Supplement 1 for supporting content.

†These authors contributed equally to this work.

REFERENCES

1. D. Zavala-Araiza, R. A. Alvarez, D. R. Lyon, D. T. Allen, A. J. Marchese, D. J. Zimmerle, and S. P. Hamburg, "Super-emitters in natural gas infrastructure are caused by abnormal process conditions," Nat. Commun. **8**, 14012 (2017).
2. A. R. Brandt, G. A. Heath, E. A. Kort, F. O'Sullivan, G. Pétron, S. M. Jordaan, P. Tans, J. Wilcox, A. M. Gopstein, D. Arent, S. Wofsy, N. J. Brown, R. Bradley, G. D. Stucky, D. Eardley, and R. Harriss, "Methane leaks from North American natural gas systems," Science **343**, 733–735 (2014).
3. S. Schwietzke, G. Pétron, S. Conley, C. Pickering, I. Mielke-Maday, E. J. Dlugokencky, P. P. Tans, T. Vaughn, C. Bell, D. Zimmerle, S. Wolter, C. W. King, A. B. White, T. Coleman, L. Bianco, and R. C. Schnell, "Improved mechanistic understanding of natural gas methane emissions from spatially resolved aircraft measurements," Environ. Sci. Technol. **51**, 7286–7294 (2017).
4. T. Lauvaux, N. L. Miles, A. Deng, S. J. Richardson, M. O. Cambaliza, K. J. Davis, B. Gaudet, K. R. Gurney, J. Huang, D. O'Keefe, Y. Song, A. Karion, T. Oda, R. Patarasuk, I. Razlivanov, D. Sarmiento, P. Shepson, C. Sweeney, J. Turnbull, and K. Wu, "High-resolution atmospheric inversion of urban CO_2 emissions during the dormant season of the Indianapolis Flux Experiment (INFLUX)," J. Geophys. Res. Atmos. **121**, 5213–5236 (2016).
5. L. C. Sinclair, I. Coddington, W. C. Swann, G. B. Rieker, A. Hati, K. Iwakuni, and N. R. Newbury, "Operation of an optically coherent frequency comb outside the metrology lab," Opt. Express **22**, 6996–7006 (2014).
6. G.-W. Truong, E. M. Waxman, K. C. Cossel, E. Baumann, A. Klose, F. R. Giorgetta, W. C. Swann, N. R. Newbury, and I. Coddington, "Accurate frequency referencing for fieldable dual-comb spectroscopy," Opt. Express **24**, 30495–30504 (2016).
7. D. T. Allen, A. P. Pacsi, D. W. Sullivan, D. Zavala-Araiza, M. Harrison, K. Keen, M. P. Fraser, A. Daniel Hill, R. F. Sawyer, and J. H. Seinfeld, "Methane emissions from process equipment at natural gas production sites in the United States: pneumatic controllers," Environ. Sci. Technol. **49**, 633–640 (2015).
8. J. L. Hall, "Nobel lecture: defining and measuring optical frequencies," Rev. Mod. Phys. **78**, 1279–1295 (2006).
9. T. W. Hänsch, "Nobel lecture: passion for precision," Rev. Mod. Phys. **78**, 1297–1309 (2006).
10. K. C. Cossel, E. M. Waxman, I. A. Finneran, G. A. Blake, J. Ye, and N. R. Newbury, "Gas-phase broadband spectroscopy using active sources: progress, status, and applications," J. Opt. Soc. Am. B **34**, 104–129 (2017).
11. I. Coddington, N. Newbury, and W. Swann, "Dual-comb spectroscopy," Optica **3**, 414–426 (2016).
12. F. Adler, M. J. Thorpe, K. C. Cossel, and J. Ye, "Cavity-enhanced direct frequency comb spectroscopy: technology and applications," Annu. Rev. Anal. Chem. **3**, 175–205 (2010).
13. A. Schliesser, M. Brehm, F. Keilmann, and D. W. van der Weide, "Frequency-comb infrared spectrometer for rapid, remote chemical sensing," Opt. Express **13**, 9029–9038 (2005).
14. T. Ideguchi, A. Poisson, G. Guelachvili, N. Picqué, and T. W. Hänsch, "Adaptive real-time dual-comb spectroscopy," Nat. Commun. **5**, 3375 (2014).
15. J. Roy, J.-D. Deschênes, S. Potvin, and J. Genest, "Continuous real-time correction and averaging for frequency comb interferometry," Opt. Express **20**, 21932–21939 (2012).
16. S. Okubo, K. Iwakuni, H. Inaba, K. Hosaka, A. Onae, H. Sasada, and F.-L. Hong, "Ultra-broadband dual-comb spectroscopy across 1.0-1.9 μm," Appl. Phys. Express **8**, 082402 (2015).
17. M. Cassinerio, A. Gambetta, N. Coluccelli, P. Laporta, and G. Galzerano, "Absolute dual-comb spectroscopy at 1.55 μm by free-running Er:fiber lasers," Appl. Phys. Lett. **104**, 231102 (2014).
18. G. B. Rieker, F. R. Giorgetta, W. C. Swann, J. Kofler, A. M. Zolot, L. C. Sinclair, E. Baumann, C. Cromer, G. Petron, C. Sweeney, P. P. Tans, I. Coddington, and N. R. Newbury, "Frequency-comb-based remote sensing of greenhouse gases over kilometer air paths," Optica **1**, 290–298 (2014).
19. E. M. Waxman, K. C. Cossel, G.-W. Truong, F. R. Giorgetta, W. C. Swann, S. Coburn, R. J. Wright, G. B. Rieker, I. Coddington, and N. R. Newbury, "Intercomparison of open-path trace gas measurements with two dual-frequency-comb spectrometers," Atmos. Meas. Tech. Katlenburg-Lindau **10**, 3295–3311 (2017).
20. L. C. Sinclair, J.-D. Deschênes, L. Sonderhouse, W. C. Swann, I. H. Khader, E. Baumann, N. R. Newbury, and I. Coddington, "Invited article: a compact optically coherent fiber frequency comb," Rev. Sci. Instrum. **86**, 081301 (2015).
21. K. C. Cossel, E. M. Waxman, F. R. Giorgetta, M. Cermak, I. R. Coddington, D. Hesselius, S. Ruben, W. C. Swann, G.-W. Truong, G. B. Rieker, and N. R. Newbury, "Open-path dual-comb spectroscopy to an airborne retroreflector," Optica **4**, 724–728 (2017).
22. P. J. Schroeder, R. J. Wright, S. Coburn, B. Sodergren, K. C. Cossel, S. Droste, G. W. Truong, E. Baumann, F. R. Giorgetta, I. Coddington, N. R. Newbury, and G. B. Rieker, "Dual frequency comb laser absorption spectroscopy in a 16 MW gas turbine exhaust," Proc. Combust. Inst. **36**, 4565–4573 (2017).
23. A. Schliesser, N. Picqué, and T. W. Hänsch, "Mid-infrared frequency combs," Nat. Photonics **6**, 440–449 (2012).
24. A. Tarantola, *Inverse Problem Theory*, 1st ed. (Elsevier Science, 1987).
25. C. B. Alden, S. Ghosh, S. Coburn, C. Sweeney, A. Karion, R. Wright, I. Coddington, K. Prasad, and G. B. Rieker, "Methane leak detection and sizing over long distances using dual frequency comb laser spectroscopy and a bootstrap inversion technique," Atmos. Meas. Tech. Discuss. (in review, 2017), DOI: 10.5194/amt-2017-262.
26. C. W. Moore, B. Zielinska, G. Pétron, and R. B. Jackson, "Air impacts of increased natural gas acquisition, processing, and use: a critical review," Environ. Sci. Technol. **48**, 8349–8359 (2014).
27. R. A. Alvarez, S. W. Pacala, J. J. Winebrake, W. L. Chameides, and S. P. Hamburg, "Greater focus needed on methane leakage from natural gas infrastructure," Proc. Natl. Acad. Sci. **109**, 6435–6440 (2012).
28. G. Pétron, A. Karion, C. Sweeney, B. R. Miller, S. A. Montzka, G. J. Frost, M. Trainer, P. Tans, A. Andrews, J. Kofler, D. Helmig, D. Guenther, E. Dlugokencky, P. Lang, T. Newberger, S. Wolter, B. Hall, P. Novelli, A. Brewer, S. Conley, M. Hardesty, R. Banta, A. White, D. Noone, D. Wolfe, and R. Schnell, "A new look at methane and nonmethane hydrocarbon emissions from oil and natural gas operations in the Colorado Denver-Julesburg Basin," J. Geophys. Res. Atmospheres **119**, 6836–6852 (2014).
29. A. P. Ravikumar, J. Wang, and A. R. Brandt, "Are optical gas imaging technologies effective for methane leak detection?" Environ. Sci. Technol. **51**, 718–724 (2017).
30. S. M. Miller, S. C. Wofsy, A. M. Michalak, E. A. Kort, A. E. Andrews, S. C. Biraud, E. J. Dlugokencky, J. Eluszkiewicz, M. L. Fischer, G. Janssens-Maenhout, B. R. Miller, J. B. Miller, S. A. Montzka, T. Nehrkorn, and C. Sweeney, "Anthropogenic emissions of methane in the United States," Proc. Natl. Acad. Sci. USA **110**, 20018–20022 (2013).
31. C. Frankenberg, J. F. Meirink, M. van Weele, U. Platt, and T. Wagner, "Assessing methane emissions from global space-borne observations," Science **308**, 1010–1014 (2005).
32. D. J. Jacob, A. J. Turner, J. D. Maasakkers, J. Sheng, K. Sun, X. Liu, K. Chance, I. Aben, J. McKeever, and C. Frankenberg, "Satellite observations of atmospheric methane and their value for quantifying methane emissions," Atmos. Chem. Phys. **16**, 14371–14396 (2016).
33. M. O. L. Cambaliza, P. B. Shepson, D. R. Caulton, B. Stirm, D. Samarov, K. R. Gurney, J. Turnbull, K. J. Davis, A. Possolo, A. Karion, C. Sweeney, B. Moser, A. Hendricks, T. Lauvaux, K. Mays, J. Whetstone, J. Huang, I. Razlivanov, N. L. Miles, and S. J. Richardson, "Assessment of uncertainties of an aircraft-based mass balance approach for quantifying urban greenhouse gas emissions," Atmos. Chem. Phys. **14**, 9029–9050 (2014).
34. S. Conley, G. Franco, I. Faloona, D. R. Blake, J. Peischl, and T. B. Ryerson, "Methane emissions from the 2015 Aliso Canyon blowout in Los Angeles, CA," Science **351**, 1317–1320 (2016).

35. H. L. Brantley, E. D. Thoma, W. C. Squier, B. B. Guven, and D. Lyon, "Assessment of methane emissions from oil and gas production pads using mobile measurements," Environ. Sci. Technol. **48**, 14508–14515 (2014).
36. T. I. Yacovitch, S. C. Herndon, G. Pétron, J. Kofler, D. Lyon, M. S. Zahniser, and C. E. Kolb, "Mobile laboratory observations of methane emissions in the Barnett Shale region," Environ. Sci. Technol. **49**, 7889–7895 (2015).
37. G. Pétron, G. Frost, B. R. Miller, A. I. Hirsch, S. A. Montzka, A. Karion, M. Trainer, C. Sweeney, A. E. Andrews, L. Miller, J. Kofler, A. Bar-Ilan, E. J. Dlugokencky, L. Patrick, C. T. Moore, T. B. Ryerson, C. Siso, W. Kolodzey, P. M. Lang, T. Conway, P. Novelli, K. Masarie, B. Hall, D. Guenther, D. Kitzis, J. Miller, D. Welsh, D. Wolfe, W. Neff, and P. Tans, "Hydrocarbon emissions characterization in the Colorado front range: a pilot study," J. Geophys. Res. Atmos. **117**, D04304 (2012).
38. J. R. Roscioli, T. I. Yacovitch, C. Floerchinger, A. L. Mitchell, D. S. Tkacik, R. Subramanian, D. M. Martinez, T. L. Vaughn, L. Williams, D. Zimmerle, A. L. Robinson, S. C. Herndon, and A. J. Marchese, "Measurements of methane emissions from natural gas gathering facilities and processing plants: measurement methods," Atmos. Meas. Tech. **8**, 2017–2035 (2015).